Fall 2017

Design and Analysis of Bio-inspired Nacelle for Current Energy Turbine

Michael Coe
San Jose State University

DESIGN AND ANALYSIS OF BIO-INSPIRED NACELLE FOR CURRENT ENERGY TURBINE

A Thesis

Presented to

The Faculty of the Department of Mechanical Engineering

San Jose State University

In Partial Fulfillment

of the Requirement for the Degree

Master of Science

by

Michael Coe

December 2017

The Designated Thesis Committee Approves the Thesis Titled

DESIGN AND ANALYSIS OF BIO-INSPIRED NACELLE FOR CURRENT ENERGY TURBINE

by

Michael Coe

APPROVED FOR THE DEPARTMENT OF MECHANICAL ENGINEERING

SAN JOSÉ STATE UNIVERSITY

December 2017

Kathryn Gosselin, Ph.D.	Department of Mechanical Engineering
Ernest Thurlow, Ph.D.	Department of Mechanical Engineering
Ken Youssefi, Ph.D.	Department of Mechanical Engineering

ABSTRACT

DESIGN AND ANALYSIS OF BIO-INSPIRED NACELLE FOR CURRENT ENERGY TURBINE

by Michael Coe

The world's oceans contain a substantial amount of energy, stored in ocean currents and waves. Ocean current energy can be extracted using similar principles to existing wind energy platforms. A problem with such extraction methods is that the velocity of the fluid in ocean currents is too low for efficient energy generation. A potential solution to this problem is the use of a concentrator or diffuser to increase fluid velocity to the blades, but this carries with it extra costs. A more cost effective solution to this problem is presented by the use of a down flow current turbine in which the body geometry can be changed to increase velocity across the turbine blades. A scale of a commercial down flow turbine is tested in a wind tunnel in order to validate CFD simulations. A biologically inspired nacelle based on the Boxfish (Ostracion cubicus) is presented and CFD simulations performed using the validated model. It is shown that by changing the body geometry of this down flow turbine, the velocity incident on the turbine blades can be increased for a given free stream velocity and such a design can cost less than a commercially available turbine.

ACKNOWLEDGEMENTS

Firstly, the author would like to acknowledge Prof. Kathryn Gosselin or allowing me to take on such a random and possibly novel topic. Secondly, I would like to thank Prof. Ernest Thurlow and Prof. Ken Youssefi for agreeing to by committee chair. Lastly, I would like to acknowledge San Jose State University for allowing me to use their facilities and software licenses.

TABLE OF CONTENTS

LIST OF TABLES

LIST OF FIGURES

1 Introduction

1.0.1 Background and Motivation

The worlds net electricity generation is predicted to increase by 69% by 2040. This corresponds to roughly 36.5 trillion kWh. The United States is predicted to increase its energy production to 18.619 trillion kWh. This increased energy generation will be supplied by 29% coal, 28% natural gas, 2% petroleum, 29% renewable sources, and 12% nuclear as shown in Fig. 1.1 [1]. Due to concerns over global warming, it is preferable to decrease the usage of the first three energy sources due to their release of greenhouse gasses into the atmosphere. Among renewable energy sources, hydroelectric

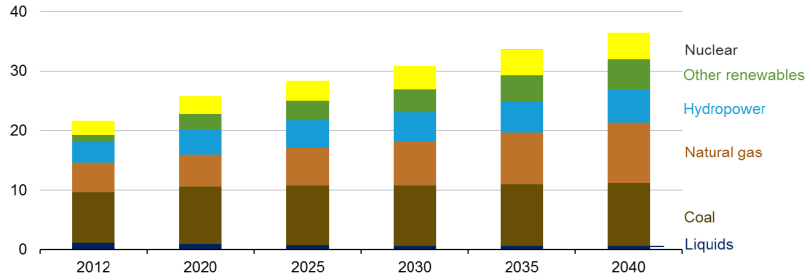

Figure 1.1: Bar chart showing the projected world energy generation sources from the International Energy Agency 2016 World Energy Outlook. The vertical axis is in trillion kilowatt hours.

sources account for about 52% (5,571 billion kWh) of the total estimated renewable sources as shown in Fig. 1.2 [1]. Of the available forms of hydroelectric energy generation, ocean current hydrokinetic turbines are an attractive option, because of the amount of energy available from the worlds oceans. The United States Department of Energy reports that the theoretical power in ocean currents around the United States is 200 TWh/year. The technical potential of these currents is between 45 and 163 $\frac{TWh}{year}$ [2]. To put this in perspective, taking the lower estimation of 45 billion $\frac{kWh}{year}$ corresponds to 0.24% of the total energy expected to be generated in the United States in the year

2040.

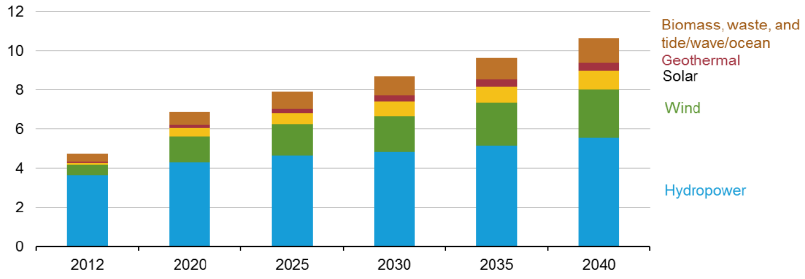

Figure 1.2: Bar chart showing the projected world energy generation from renewable sources from the International Energy Agency 2016 World Energy Outlook. The vertical axis is in trillion kilowatt hours.

One reason that the fraction of energy from ocean currents being low is due to many ocean currents being below $2\frac{m}{s}$. Fig. 1.3 shows the trends for currents over a 24 period. These currents were taken off the coast of San Francisco, California from the National Data Buoy Center [3]. The figures show that the current velocity over the 24 hour period never increases above $1\frac{m}{s}$.

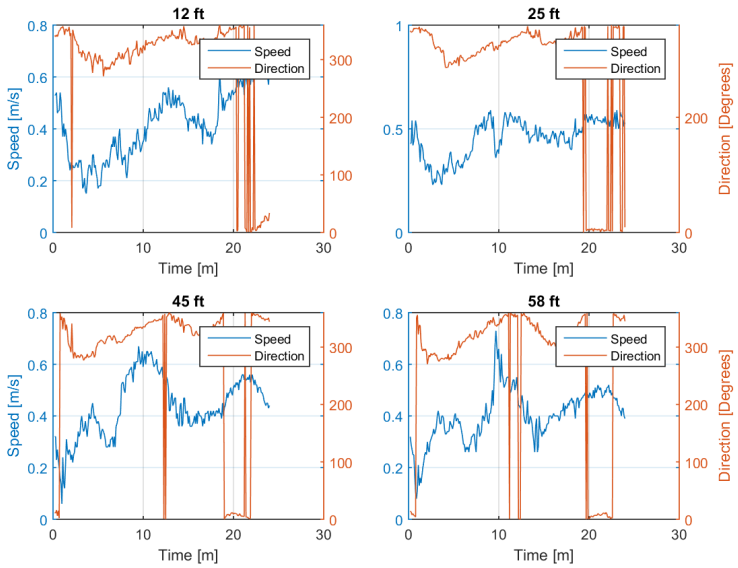

Figure 1.3: The speed and direction for ocean current outside of San Francisco, California on Jul, 26th 2012 taken from the National Data Buoy Center

There are two methods to increase the power of turbines. One method is to increase the swept area of the turbine. This method causes construction and placement concerns, and the power only increases linearly with swept area. The power of a turbine increases with velocity cubed, and the second method seeks to increase local velocities at the blades. This method employs the use of a duct or diffuser to increase local velocities. The diffuser acts like a nozzle in that it decreases the area from the turbine inlet to the blades. This causes the velocity of the fluid to increase into the blades [4].

1.0.2 Objectives

The objective of this thesis is to design a turbine nacelle that functions similar to a duct or diffuser. The increase in velocity will be facilitated by only nacelle geometry, which incorporates bio-inspired analogues. This will allow marine current turbines to generate adequate electricity in lower flow currents. Furthermore, by making small changes to the nacelle geometry, the overall cost of the turbine is decreased with respect to turbines with diffusers.

2 Literature Review

There are two types of devices to extract energy from water, hydrostatic and hydrokinetic. Hydrostatic methods involve building dams in order to create a pressure difference between the dammed reservoir and downstream to drive turbines. The hydrokinetic approach uses the flow water as a working fluid to directly drive a turbine, similar to that of a conventional wind turbine [5]. The hydrostatic approach is historically the most common, but in the past decade, considerable research and attention has been given to hydrokinetic energy generation.

Hydrokinetic methods can be divided into two categories: current-based and wave-based. Among current-based methods, water currents are divided into four categories: river, tidal, ocean, and irrigation and other man made canals [6]. Of these categories, tidal and ocean currents contain the greatest power density. This thesis will focus on the hydrokinetic method of tidal and ocean currents for energy generation.

The types of hydrokinetic turbines used for tidal and ocean currents can be characterized by their rotational axis orientation with respect to water flow direction [6]. This is analogous to wind turbines and results in the same two types: horizontal axis and vertical axis. Of these two, the horizontal axis marine current turbine (HAMCT) is the most technologically and economically viable option [7], because it is based on existing wind turbine technologies, which is a heavily researched and mature field.

2.1 A Brief History of HAMCT

The use of water currents for the generation of useful work can be traced back to Vitruvius in the Augustan Age (31 BC to AD 41). This was the first description of a water wheel. Water power, in the form of water wheels, was employed throughout China and Europe to grind grain [8]. The water wheel did not become a water turbine

until around 1832, when a French engineer by the name of Benoit Fourneyron patented the first such device. This turbine used guide vanes to direct water towards runner blades that deflected the water to cause rotational motion [8].

Soon after Fourneyrons development, James Bicheno Francis, a British-American engineer developed an inward flow radial turbine. The modern turbine can be attributed to Victor Kaplan. He invented the Kaplan turbine in 1913. This was the first propeller type machine which was an evolution of the Francis turbine. These modern turbines convert energy of a stream of fluid into mechanical energy by passing the stream through blades and causing a rotational motion [8].

2.2 Advantages

When discussing advantages and disadvantages, it's useful to compare conventional horizontal axis wind turbines (HAWT) and HAMCT. The advantages of HAMCT are that water has a greater power density than air, tides and currents are predictable and forecastable, and HAMCT has a minimal visual impact [6].

The power generated from an HAMCT is analogous to wind power. The relevant equation is:

$$P = K\frac{1}{2}\rho A v^3$$

where K is the power coefficient of the turbine, ρ is the density of water, A is the swept area given by $A = \frac{1}{4}\pi D^2$ where D is the diameter of the blades, and v is the speed of the incoming fluid [6], [8]. There is a theoretical limit to the amount of kinetic energy that can be converted by the turbine to energy. This limit is the known as the Betz limit and is given as 59.3% [6]. A typical wind turbine is rated at around $11\frac{m}{s}$ wind speed while a HAMCT is normally rated at $2\frac{m}{s}$. Furthermore, typical density for air is $1.225\frac{kg}{m^3}$ and for sea water $1025\frac{kg}{m^3}$. Assuming that both turbines are operating at the Betz limit, the difference in power between the two types of turbines can be calculated.

Table 2.1 shows this comparison between HAWT and HAMCT.

Table 2.1: Power generated by wind and marine current turbines at different diameters.

Diameter [m]	HAWT at $11\frac{m}{s}$	HAMCT at $2\frac{m}{s}$
5	18.29 kW	95.48 kW
10	73.15 kW	381.91 kW
15	164.58 kW	859.29 kW

A further advantage of marine current energy is that the energy extracted is predictable. Ocean current is directly related to the tides, which are pulsing energy sources that give maximum flow about every six hours and thirteen minutes. However, between two peaks, there is a minimum of flow which gives little energy production. To deliver commercial power, low variation in energy production is preferred [9]. Since peak power production can be predicted, it is easier to mitigate the effects of this large variation. It is important to note that different locations will experience different peak current velocities at different times of day. This difference in phase between locations can compensate for the variation in peak power extraction [9]. As noted in Giorgi and Ringwood, due to tides astronomical nature, the time evolution of tides can be predicted up to a decade with great accuracy. This deterministic property makes tidal current energy attractive when compared to other renewable energies. Renewable energies such as solar and wind can not be predicted with such accuracy.

A final advantage that has not gotten much attention is the size comparison between a marine current turbine (MCT) and a wind turbine. Due to the greater power density, MCTs are not required to be as large for the same power rating. As described in Elghali *et al.*, an offshore wind turbine rated for 1 MW has a diameter of 55 meters, while a MCT with the same rating has a diameter of 18 meters [10]. Fig. 2.1 gives a representation of these two turbines side-by-side.

In order to examine the benefit of this size difference, it is assumed that each turbine

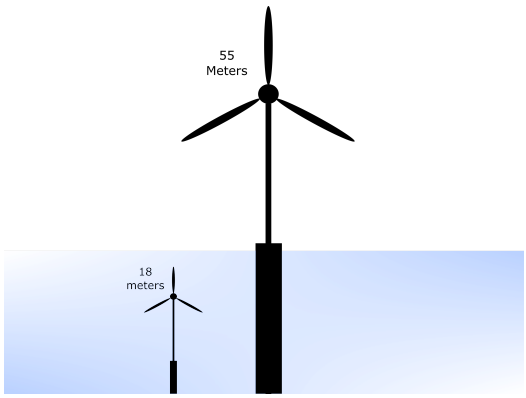

Figure 2.1: Comparison between an horizontal axis wind turbine and a horizontal axis marine current turbine at dimensions specified by Elghali *et al.*

runs at 30% efficiency. The power generated by each turbine is calculated for velocities ranging from 0 to $2\frac{m}{s}$ for the marine current turbine and 0 to $15\frac{m}{s}$. The marine turbine was kept at an 18 m diameter and a wind turbine at 18 meters and 55 meters were used. Fig. 2.2 shows the results of these calculations.

The figure shows that each turbine reaches the roughly the same power generation at different velocities. The data shows that the 18 meter wind turbine must have almost $14\frac{m}{s}$ before reaching the same power generation as the marine current turbine. When switched to 55 meters, the wind turbine needs a fluid velocity of $7\frac{m}{s}$ compared to the approximately $2\frac{m}{s}$.

Further contributing to this size difference is the size of the foundation. For a typical offshore wind turbine not only is the tower needed, but a solid gravity anchor to the seabed is required. This anchor is usually concrete and has to be made large enough to support the wind turbine as well as withstand oncoming currents. This contrasts with a MCT because the tower and anchor of an MCT can be made much smaller and only has to support the forces of the oncoming current and moment generated by the turbine blade. This drastically reduces the support structure costs making MCTs attractive from an economical standpoint.

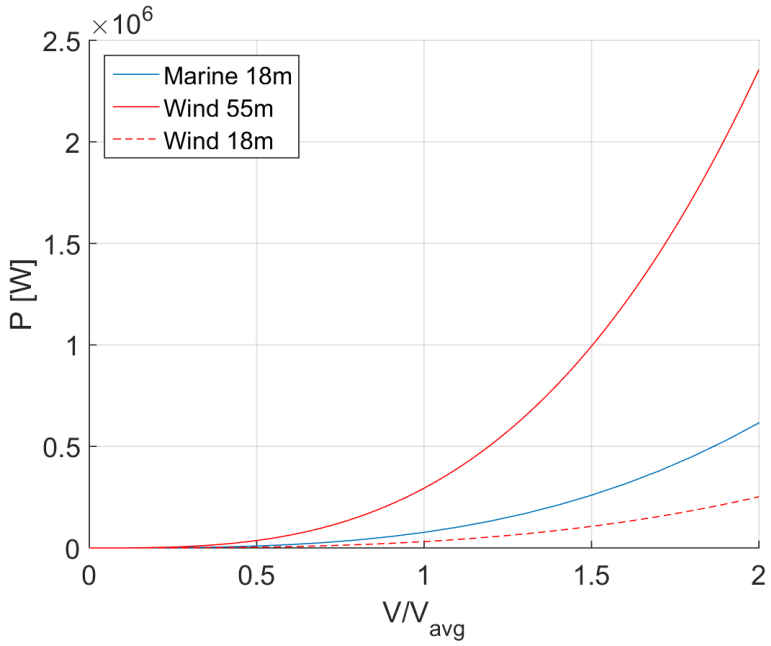

Figure 2.2: Power comparison for marine current turbine at 18 m diameter and wind turbine at 18 m and 55 m diameter.

2.3 Disadvantages

An obvious disadvantage to marine current turbines is the environment in which they operate. When discussing the ocean environment with respect to marine current turbines, there are two aspects that are of particular interest: the metal corrosive environment of seawater and the environmental impact.

Seawater contains salts, dissolved gasses, moving sand, and dead organisms. These combine to create a very corrosive environment [11]. With respect to metals used in MCTs, the salt and oxygen content of seawater is the main concern. Concerning salt, changes in salinity will cause a change in the conductivity in seawater. Since corrosion is caused by a difference in electric potential, this change in conductivity will contribute to the corrosion of metal components [11].

A greater concern is the amount of dissolved oxygen suspended in seawater. Most of the corrosion observed in submarines is caused by oxygen depolarization. This affects

components made out of steel and copper [11] which would pertain to the structural and electricity generation aspects of the MCT. There has been a fair amount of research pertaining to mitigation of the corrosion of metal parts in seawater such as using special polymer paints and primers that preclude corrosion. Other research has been focused on using corrosion resistant composites in place of metals [11].

Pertaining to biological considerations, the only environmental impact study to date was performed by marine current turbines in the United Kingdom. The report concluded that there is no significant change to mammals and benthic seabed communities at the turbine sites. The report further concluded that there was colonization of the turbine foundation, mostly by barnacles and crabs [12]. This colonization is known as bio-fouling and occurs on the outer hull of ships as well.

Bio-fouling can cause significant problems with drag over the surface of a marine structure. This is particularly important for free flow or down flow marine current turbines. The reason for this is that the fluid must flow over the nacelle of the turbine before reaching the blades. Any sort of disruption in the hydrodynamic flow field in this area can have a significant impact on turbine performance.

In addition to bio-fouling, local seabed scour presents a significant problem [7]. This would only affect MCTs that utilize gravity anchors or foundations. Scour occurs when a marine structure foundation changes the local hydrodynamics at the seabed. This usually causes an increase in flow velocity which in turn increases the sediment transport away from the foundation. The loss of sediment causes instabilities in the turbine base and would need to be researched further and mitigated [7].

2.4 Categories of Research

According to Ng *et al.*, there are six research areas pertaining to tidal energy extraction: energy assessment, turbine design, wakes, generators, novel modifications, and environmental impact.

2.4.1 Energy Assessment

In order to deploy arrays of HAMCT at the scale which is required for commercial power generation, the energy resources available at a particular site must be assessed. As stated before, the maximum theoretical energy extracted by ocean current is given by $P = K\frac{1}{2}\rho A v^3$ and is governed by the Betz limit of 59.3%. It is important to understand that the Betz limit is actually adapted from wind turbines and makes the assumption that the turbine is removing energy from unconstrained, incompressible flow which has no interactions around the site [13].

In reality, marine currents and wind are time variant. Bryden *et al.* developed a general energy extraction model that includes variation in flow speed and direction as a function of time for currents. It is important to note that the horizontal speed of tidal flows vary based on their height above the seabed. Their model is given for a hub as a function of the height of the hub above the seabed as follows [13]:

$$[\overline{u^3}]^{\frac{1}{3}} = \frac{4}{\pi D^2}\int_{-D/2}^{D/2} \cos[\sin^{-1}\left(\frac{2y}{D}\right)]u^3(y+z_o)dy$$

where D is the diameter of the swept area, z_o is height of the center of the hub above the seabed. Bryden *et al.* explained that their model is a simple one channel model that could potentially overestimate the maximum energy flux [13].

In contrast to Bryden *et al.*, Garret and Cummins developed a model where the flow is driven by a pressure gradient vise a static head difference [7]. Their model makes the assumptions that the channel does not change cross section with time and is uniform from the entrance to the exit. Furthermore, the current speed is uniform and the tidal elevation are constant and unaltered by the presence of the turbine [14]. Their model is formulated as follows [14]:

$$P_{max} = 0.38\rho Q_0 g\zeta_0$$

where Q_0 is the volume flux with no turbines and ζ_o is the sinusodal tidal forcing $\zeta_0 = a\cos wt$. This can be changed to include a channel of varying cross section by introducing a correction factor α as follows [14]:

$$P_{max} = 0.38(1+\alpha)\ x\ \frac{1}{2}\rho A_e |u_{e0}|^3$$

where α is given by $2A_e^2 \int_0^L C_d(hA^2)^{-1}dx$, u_{e0} is the exit speed with no turbine present, C_d is the drag coefficient, h is the cross-sectionally averaged water depth, and A_e is the cross sectional area of the channel exit. With this model, it is found that maximum power can be calculated as approximately 10% of the peak tidal pressure head multiplied by the peak volume flux [7].

2.4.2 Turbine Design

Turbine design mainly focuses on the performance of the HAMCT, and, in particular, the performance of the turbine blade. The work of Prof. Bahaj's group at University of Southhampton has focused on the lift, drag, and cavitation of two-dimensional foil sections [7]. To verify their results, an 800-mm-diameter HAMCT with three blades was constructed and analyzed in a cavitation tunnel [15].

Bahaj *et al.* found that there is a consistent power and thrust decrease with increasing yaw angle with respect to fluid inflow. Furthermore, they found that power production for shallow tip immersion (where the turbine is close to the water surface) is approximately 10-15% lower than with deep tip immersion. The group further reported that with careful designs of blade angles and tip speed, cavitation can be mitigated in large scale HAMCTs [15]. Lastly, they were able to extend the Blade Element Momentum (BEM) method in order to match their experimental data [16].

There are many commercial variants to the HAMCT, but producers are less forthcoming with information. Of note, SeaGen turbine by Marine Current Turbines is the first, largest attempt at in-stream hydrokinetic energy. Their design is a twin HAMCT with

bi-directional two bladed propellers that span 18 meters in diameter each. These turbines are mounted on a 21 meter high steel structure that is anchored to the seabed [5]. The second commercial turbine of note is made by Verdant Power and feathers a three-bladed rotor with a 5 meter diameter. These turbines feature a constant rotational speed of 40 rpm and boast an efficiency of between 0.38 and 0.44 [5]. This turbine is outlined later in this review.

2.4.3 Wakes

In order to place MCTs in an array to create a turbine farm, it is important to understand how the wakes of adjacent turbines affect the flow to the turbine blades. In this realm of research, Bahaj *et al.*, mentioned above, has done much research. Their experiment used a cavitation tunnel with a 1/30th scale turbine mounted inside. Using this cavitation tunnel, the wake field can be measured and analyzed with various hydrodynamic flows [17].

The conclusions of their research is that the wake length increases the further immersed the turbine blade is. Furthermore, the reason for a smaller wake with a shallow tip immersion is due to the free surface acting as a reflection plane. It is important to note that due to this reflection, there is little change in the thrust of the turbine, but a large reduction in power is observed [17].

To understand the effect of two turbines together, Bahaj *et al.* used the cavitation tunnel in a dual rotor test. The rotors were placed side by side and tested with different horizontal gaps. Furthermore, the second rotor (referred to as dummy rotor in their research) was tested in both static and rotating configurations. The group found that even at very small gaps, there is very little interference from the dummy rotor [17].

2.4.4 Generators

Research into generators is focused on producing constant electricity. The reason for this is that ocean current velocity fluctuates continuously as $\zeta_0 = a\cos wt$. Ben Elghali *et al.* has been active in researching different generator models. They developed a Matlab-Simulink model that they have validated for doubly-fed induction generators (DFIG), permanent magnet synchronous generators (PMSG), and variations of those two. It is common for large-scale HAMCTs to use induction generators [7].

2.4.5 Turbine Modifications

Modifying the design of a HAMCT to increase performance falls into two categories: changing of body design and changing of rotor design. In the realm of body design, researchers have examined using diffusers to increase the inflow velocity to the turbine. A diffuser is a nozzle decreases the area of the inlet to the turbine over a specific length. This causes the flow velocity to increase before it hits the turbine blade.

The advantages to using a diffuser is that the turbine can extract the same amount of energy for a smaller size and it can be used to eliminate torque on the main power shaft. This is achieved by using the blades as magnets and installing stator and windings in the duct. The disadvantages to using a diffuser is that the blades require very small clearances between the shroud and the blade tip, the turbine operates at higher RPMs which causes vibration in the housing, and there is more of a drag force on the turbine [18].

There are two types of diffuser shapes: rectilinear and annular ring. Currently, only CFD analysis of diffuser shapes and their relative performance is available due to their emerging nature and high start up costs [18]. Shives and Crawford [19] have developed an empirical model for a ducted turbine. They state that the mass flow increase by the duct is influenced by four factors: the diffuser area ratio $\left(\frac{A_2}{A_1}\right)$ where A_2 is the outlet

area and A_1 is the inlet area, the degree of flow separation from the diffuser surface, the base pressure reduction at the diffuser exit caused by the obstruction of flow, and the viscous losses within the entire duct [19].

It was found that the diffuser efficiency decreased with increasing diffuser expansion, inlet contraction, and inner exit angle. These results show that boundary layer flow control may have greater importance in practical designs. In particular, the group found that the maximum performance happens when balancing the increasing base pressure effect with the loss from decreased diffuser efficiency. According to their conclusions, a flanged rectilinear diffuser creates a large base pressure is the most desirable type of diffuser [19].

2.5 Current Problems with HAMCT

One of the biggest problems with marine current turbines is cavitation. Cavitation happens with the formation of water bubbles or voids when the local pressure of a volume of water falls below the vapor pressure [5]. This occurs in marine current turbines due to the change in pressure created by the moving blade. The bubbles or voids formed can explode or implode causing shock waves which impart force on the turbine blade and causes cyclic stress.

Another problem with HAMCT is that the systems have small scale power production with low power coefficients when compared to horizontal axis wind turbines [5]. The reason for this, discussed in the advantages section, is the Betz limit. The Betz limit states that the maximum theoretical efficiency of the turbine is 59.3%. The highest efficiency reached thus far is 50% from commercial systems [5].

A final problem with HAMCT is the leakage of lubricant, noise, and vibration caused by the turbine [5]. There has been little study to the adverse effect to the marine habitat of the above problems. The only study done to the authors knowledge was performed by the commercial company Marine Current Turbines LLC. This company concluded

that there is no discernable effect to marine wildlife due to noise or vibration [12]. This environmental study did not measure the lubrication leakage from their turbine, so no data is present pertaining to this problem and further scientific inquiry is needed.

2.6 Numerical and CFD Methods Used

2.6.1 Flow Models

In general, flow around a fixed body is governed by the continuity and Navier Stokes equations. These equations are as follows [20]:

$$\frac{\partial \rho}{\partial t} + u\frac{\partial \rho}{\partial x} + v\frac{\partial \rho}{\partial y} + w\frac{\partial \rho w}{\partial z} = 0$$

$$\rho\left(\frac{\partial u}{\partial t} + u\frac{\partial u}{\partial x} + v\frac{\partial u}{\partial y} + w\frac{\partial u}{\partial z}\right) = -\frac{\partial P}{\partial x} + \mu\left(\frac{\partial^2 u}{\partial x^2} + \frac{\partial^2 u}{\partial y^2} + \frac{\partial^2 u}{\partial z^2}\right) + X$$

$$\rho\left(\frac{\partial v}{\partial t} + u\frac{\partial v}{\partial x} + v\frac{\partial v}{\partial y} + w\frac{\partial v}{\partial z}\right) = -\frac{\partial P}{\partial y} + \mu\left(\frac{\partial^2 v}{\partial x^2} + \frac{\partial^2 v}{\partial y^2} + \frac{\partial^2 v}{\partial z^2}\right) + Y$$

$$\rho\left(\frac{\partial w}{\partial t} + u\frac{\partial w}{\partial x} + v\frac{\partial w}{\partial y} + w\frac{\partial w}{\partial z}\right) = -\frac{\partial P}{\partial z} + \mu\left(\frac{\partial^2 w}{\partial x^2} + \frac{\partial^2 w}{\partial y^2} + \frac{\partial^2 w}{\partial z^2}\right) + Z$$

where ρ represents the density. u, v, and w are the velocities in the x, y, and z directions. P is the pressure and X, Y, Z are the body forces on the fluid in the x, y, and z directions. Furthermore, the stresses on the fluid are defined in the following manner [20]:

$$\sigma_x = P - 2\mu\frac{\partial u}{\partial x} + \frac{2}{3}\mu\left(\frac{\partial u}{\partial x} + \frac{\partial v}{\partial y}\right)$$

$$\tau_{xy} = \mu\left(\frac{\partial u}{\partial y} + \frac{\partial v}{\partial x}\right)$$

2.6.2 Time / Reynolds Averaged Navier Stokes Equation

When using Computational Fluid Dynamics (CFD) over a bluff body, the general consensus is to use a Reynolds Averaged Navier Stokes (RANS) formulation [21] [22]. In order to time average the above equation, Reynolds decomposition is used. This is the separation of the components into time averaged and fluctuating parts as follows

[20]:

$$u = \bar{u} + u', v = \bar{v} + v'$$

$$w = \bar{w} + w', P = \bar{P} + P'$$

where the bar represents the time averaged value and the primed value represents the fluctuation about the average value. A special property used in this formulation is that the fluctuations averaged over time equal zero or [20]:

$$\int_0^t u' dt = 0$$

From these definitions, we get the following rules [20]:

$$\overline{u+v} = \bar{u} + \bar{v}$$

$$\overline{\bar{u}u'} = 0$$

$$\overline{uv} = \bar{u}\bar{v} + \overline{u'v'}$$

$$\overline{u^2} = \bar{u}^2 + \overline{u'^2}$$

$$\overline{\frac{\partial u}{\partial x}} = \frac{\partial \bar{u}}{\partial x}$$

$$\overline{\frac{\partial \bar{u}}{\partial t}} = 0$$

$$\overline{\frac{\partial u}{\partial t}} = 0$$

with all these rules applied to the Navier Stokes equation, the time dependence is removed and the momentum equations can be written as follows [20]:

$$\bar{u}\frac{\partial \bar{u}}{\partial x} + \bar{v}\frac{\partial \bar{u}}{\partial y} + \bar{w}\frac{\partial \bar{u}}{\partial z} = -\frac{1}{\rho}\frac{\partial \bar{P}}{\partial x} + \nu\nabla^2\bar{u} - \frac{\partial}{\partial x}(\overline{u'^2}) - \frac{\partial}{\partial y}(\overline{u'v'}) - \frac{\partial}{\partial z}(\overline{u'w'})$$

$$\bar{u}\frac{\partial \bar{v}}{\partial x} + \bar{v}\frac{\partial \bar{v}}{\partial y} + \bar{w}\frac{\partial \bar{v}}{\partial z} = -\frac{1}{\rho}\frac{\partial \bar{P}}{\partial y} + \nu\nabla^2\bar{v} - \frac{\partial}{\partial x}(\overline{u'v'}) - \frac{\partial}{\partial y}(\overline{v'^2}) - \frac{\partial}{\partial z}(\overline{v'w'})$$

$$\bar{u}\frac{\partial \bar{w}}{\partial x} + \bar{v}\frac{\partial \bar{w}}{\partial y} + \bar{w}\frac{\partial \bar{w}}{\partial z} = -\frac{1}{\rho}\frac{\partial \bar{P}}{\partial z} + \nu\nabla^2\bar{w} - \frac{\partial}{\partial x}(\overline{u'w'}) - \frac{\partial}{\partial y}(\overline{v'w'}) - \frac{\partial}{\partial z}(\overline{w'^2})$$

These 4 equations take care of the fluid flow around an object, but do not account for eddy-viscosity turbulence. Eddy-viscosity turbulence is the transfer of momentum that is caused by turbulent eddies. This was first postulated by Joseph Boussinesq in 1877. The most common models of eddy-viscosity are known as the two-equation models. The most common of these are the k-ε and k-ω models.

2.6.3 k-ω

Of the two-equation turbulence models, the k-ω is used extensively. Specifically, the Shear-Stress Transport (SST) k-ω model [23] is the focus of this thesis. This model was first presented by [23] and takes advantage of the Wilcox k-ω model in the near wall region and transforms the k-ε into a k-ω formulation for values outside the boundary layer. A short derivation is as follows:

The original k-ω model is written as follows [23]:

$$\frac{D\rho k}{Dt} = \tau_{ij}\frac{\partial u_i}{\partial x_j} - \beta^*\rho\omega k + \frac{\partial}{\partial x_j}\left[(\mu + \sigma_{k1}\mu_t)\frac{\partial k}{\partial x_j}\right]$$
$$\frac{D\rho\omega}{Dt} = \frac{\gamma_1}{\nu_t}\tau_{ij}\frac{\partial u_i}{\partial x_j} - \beta_1\rho\omega^2 + \frac{\partial}{\partial x_j}\left[(\mu + \sigma_{w1}\mu_t)\frac{\partial w}{\partial x_j}\right]$$

Where $\frac{D}{Dt} = \frac{\partial}{\partial t} + u_i\frac{\partial}{\partial x_i}$. $\tau_{ij} = \mu_t(\frac{\partial u_i}{\partial x_j} + \frac{\partial u_j}{\partial x_i} - \frac{2}{3}\frac{\partial u_k}{\partial x_k}\delta_{ij}) - \frac{2}{3}\rho k\delta_{ij}$, $\nu_t = \frac{k}{\omega}$. $\sigma_{k1/2}$, $\sigma_{\omega 1/\omega 2}$, $\beta_{1/2}$, β^*, k, and $\gamma_{1/2}$ are all constants specified in [23]. The transformed k-ε model is as follows [23]:

$$\frac{D\rho k}{Dt} = \tau_{ij}\frac{\partial u_i}{\partial x_j} - \beta^*\rho\omega k + \frac{\partial}{\partial x_j}\left[(\mu + \sigma_{k2}\mu_t)\frac{\partial k}{\partial x_j}\right]$$
$$\frac{D\rho\omega}{Dt} = \frac{\gamma_2}{\nu_t}\tau_{ij}\frac{\partial u_i}{\partial x_j} - \beta_2\rho\omega^2 + \frac{\partial}{\partial x_j}\left[(\mu + \sigma_{w2}\mu_t)\frac{\partial w}{\partial x_j}\right] + 2\rho\sigma_{w2}\frac{1}{\omega}\frac{\partial k}{\partial x_j}\frac{\partial \omega}{\partial x_j}$$

In order to account for the transition from one model to another, a blending function

F_1 is used. This is defined as:

$$F_1 = \tanh\left(\min\left[\max\left(\frac{\sqrt{k}}{0.09\omega y}; \frac{500\nu}{y^2\omega}\right); \frac{4\rho\sigma_{w2}k}{CD_{kw}y^2}\right]\right)$$

$$and$$

$$CD_{k\omega} = \max\left(2\rho\sigma_{w2}\frac{1}{\omega}\frac{\partial k}{\partial x_j}\frac{\partial \omega}{\partial x_j}, 10^{-20}\right)$$

This function is multiplied by the k-ω model and (1-F_1) is multiplied by the k-$epsilon$ model. The two models are then added together to become [23]:

$$\frac{D\rho k}{Dt} = \tau_{ij}\frac{\partial u_i}{\partial x_j} - \beta * \rho\omega k + \frac{\partial}{\partial x_j}\left[(\mu + \sigma_k\mu_t)\frac{\partial k}{\partial x_j}\right]$$
$$\frac{D\rho\omega}{Dt} = \frac{\gamma}{\nu_t}\tau_{ij}\frac{\partial u_i}{\partial x_j} - \beta\rho\omega^2 + \frac{\partial}{\partial x_j}\left[(\mu + \sigma_w\mu_t)\frac{\partial w}{\partial x_j}\right] + 2\rho\left(1 - F_1\right)\sigma_{w2}\frac{1}{\omega}\frac{\partial k}{\partial x_j}\frac{\partial \omega}{\partial x_j}$$

2.6.4 Blade Numerical Models

The classical theory is also known as the Actuator Disk Method (ADM). The area swept by the turbine blades are represented by an ideal actuator disk. This disk is frictionless and has no rotational velocity component in the wake [24]. With this formulation, this case can be analyzed in one dimension. The induced velocities u and u_1 at the disc and the wake are written as [24]:

$$V_0 - v = u = (1 - a)V_0 \tag{2.1}$$

$$V_0 - v_1 = u_1 = (1 - 2a)V_0 \tag{2.2}$$

where $v = aV_0$ and $v_1 = 2aV_0$, V_0 is the speed of the incoming fluid, and a is the axial induction factor defined as $a = 1 - \frac{u}{V_0}$.

From this, the thrust and power coefficients can be obtained by applying energy conservation on the control volume. Taking T to be the kinetic power defined as $T = \dot{m}(V_0 - u_1)$ and P as the kinetic power defined as $P = \frac{1}{2}\dot{m}(V_0^2 - u_1^2) = Tu$. The

resulting coefficients are [24]:

$$C_T = \frac{T}{\frac{1}{2}\rho A V_0^2} = 4a(1-a) \tag{2.3}$$

$$C_P = \frac{P}{\frac{1}{2}\rho A V_0^3} = \frac{Tu}{\frac{1}{2}\rho A V_0^3} = 4a(1-a)^2 \tag{2.4}$$

2.6.5 Blade Element Method (BEM)

The Blade Element Method (BEM) is based on Blade Element Theory and was introduced by Glauert in 1963 [24]. This method models the rotating turbine blade as a fluid sub-domain that occupies the disk thats swept by a complete rotation of the turbine blades [25]. This is accomplished by sectioning the entire blade span and then calculating lift and drag forces on each section based on the local angle of attack, chord length, and airfoil shape [25]. The effect of the rotating blade is simulated by a body force calculated on the fluid equal and opposite to the lift and drag on each blade element. This is then averaged over a full revolution.

The induced velocity on each individual element is given by $W_z = V_0 - u$. The balance of the axial momentum is given by [24]:

$$\Delta T = 2W_z \Delta \dot{m} \tag{2.5}$$

where $\Delta \dot{m} = \rho(V_0 - W_z)\Delta A$. The corresponding angular momentum balance in terms of the induced angular velocity W_θ is given by [24]:

$$\Delta Q = 2W_\theta r \Delta \dot{m} \tag{2.6}$$

The momentum must be balanced with hydrodynamic forces on the blades. In order to accomplish this, the cross section of the hydrofoil is taken at radius r in the (θ, z) plane. Fig. 2.3 shows the blade element with relevant vector geometry.

The relative velocity to the hydrofoil element is given by the velocity triangle as

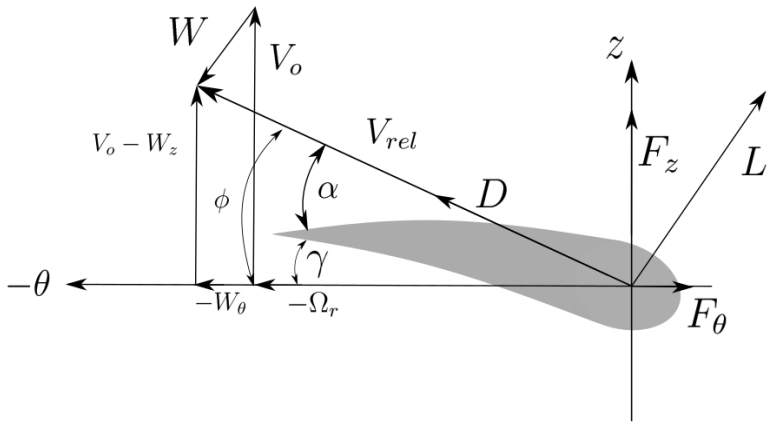

Figure 2.3: Cross section of blade element showing velocity components.

$V_{rel}^2 = (V_0 - W_z)^2 + (\Omega r + W_\theta)^2$, where Ω is the angular velocity [24]. The flow angle ϕ is the angle between the V_{rel} and the rotor plane and is given by [24]:

$$\phi = \tan^{-1}\left(\frac{V_0 - W_z}{\Omega r + W_\theta}\right) \tag{2.7}$$

from this, the local angle of attack can be calculated using $a = \phi - \gamma$, where γ is the local pitch angle [24].

In order to calculate the lift and drag forces per the chord length, the formula given by [25] is used:

$$f_{L,D} = c_{L,D}(\alpha, Re)c(r/R)\frac{\rho V_{tot}^2}{2} \tag{2.8}$$

here, the lift or drag coefficient is given by $c_{L,D}$ which depends on angle of attack (α) and Reynolds number (Re). These numbers are taken from tabulated data. $c(r/R)$ is the chord length of the blade section, ρ is the air density, and V_{tot} is the velocity of the fluid relative to the blade.

The directions of lift and drag are not uniform throughout the span. Instead, the values are governed by unit vectors $\hat{e}_L$ and $\hat{e}_D$. The force per unit chord length is given by $\vec{F} = \vec{L} + \vec{D}$. Projecting this force into the axial and tangential direction to the rotor

gives the following components [24]:

$$F_z = Lcos\phi + Dsin\phi, \quad F_\theta = Lsin\phi - Dcos\phi \tag{2.9}$$

and since these forces balance the momentum changes in the axial and tangential directions, the momentum changes become [24]:

$$\Delta T = F_z \Delta r, \quad \Delta Q = F_\theta r \Delta r$$

The induced velocities and blade forces are found using an iterative method. It is important to note that the BEM method uses the assumptions of axial symmetry, inviscid flow, radially independent elements, that the induced velocity on the disc equals one half the induced velocity in the far wake, and conservation of circulation is ignored [24].

2.7 Biological Analogues

There has been a fair amount of research into the hydrodynamics of fish. A majority of the early research was performed by Lighthill [26]. Lighthill's study pertains to fish that utilize lateral undulations as a mode for swimming. Undulatory swimmers are further broken into two classes: anguilliform and carangiform. Anguilliform fish are those in which the whole body undulates while swimming while carangiform fish only use their posterior undulations for propulsion. It is noted that a compression, or flattening of the cross-section into a posterior edge, at the posterior end in both classes of fish improves their hydromechanical efficiency [26].

2.7.1 Hydrodynamics of Swimming Fish

Triantafyllou *et al.* expanded Lighthill's observation on vortex shedding by fins [27]. It is stated that fish use vorticity control by way of their fins in order to produce thrust. As noted by Triantfyllou *et al.*, this occurs in the following three ways [27]:

1. Interact constructively to generate stronger vortices in the wake.

2. Interact destructively to generate weaker vortices in the wake.
3. Pair with opposite sign vortex generating vortex pairs that drift away from the fish center line. This creates a wide wake.

It is found that flow downstream of a foil can be characterized by the formation of a wake that has two or four large vortices per period. Triantafyllou *et al.* finds that high propulsive efficiency is associated with a reverse Kármán street behind a bluff body [27]. A Kármán street is a staggering of two vortices per cycle that rotate in the same direction. A reverse Kármán street is a staggering of two vortices per cycle but with both vortices rotating in the opposite direction.

Triantafyllou *et al.* [27] gives the following process of fish vorticity control: The body motion has the form of a traveling wave along the fish. The generates spatially traveling waves of body-bound vorticity intersecting at right angles to the transverse motion of the fish. The flow is strongest near the upper and lower edges of the fish. This means that there is two-dimensional flow in some planes and not in others. This can be seen in the Fig. 2.4. This figure shows shows how a fish can reorient it's body and tail to create destructive interference between oncoming vortices and it's own body vortices. The result is a reverse Kármán street that increases propulsive efficiency.

The following process is explains the propagation of the vortex along the fish body [27]: The amplitude of the body motion increases from head to tail which causes the vorticity amplitude to increase. When the lateral amplitude reaches a maximum width, the vortices at the upper and lower edges are shed into the wake at the mid-length region. These vortices start weak, but grow stronger as they reach the peduncle region. Once in the peduncle region, the vortices are re-positioned by the tail from the fish's left side to its right side, and from the fish's right side to its left side. This vortex shedding depends strongly on the form of the fish and shape of the fins.

So far, the information presented on fish hydrodynamics applies to fish which swim

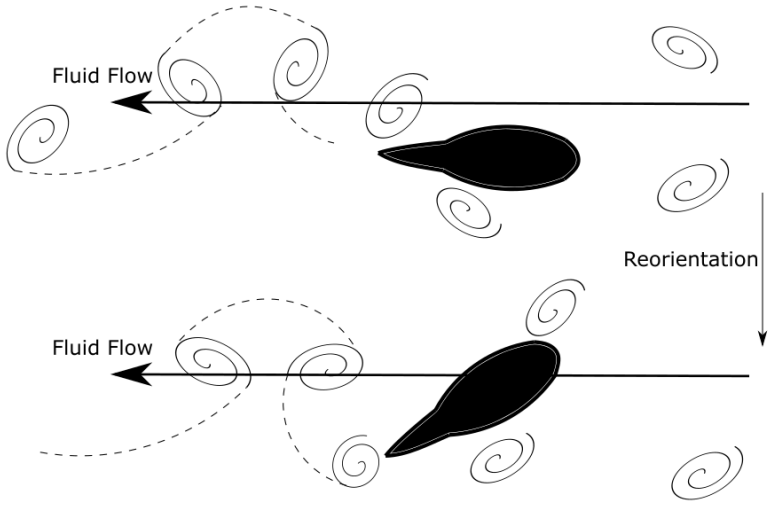

Figure 2.4: Flow visualization of fish manipulating incident fluid flow. Vortices are re-positioned by the body and tail to create destructive interference with fish generated vorticity. The results are a reverse Kármán street in the wake.

using undulation of their body. Due to the nature of a marine current turbine, it is more beneficial to explore hydrodynamics of rigid bodies. Fish in the family Ostraciidae, in particular, have rigid bodies and use their fins to re-position vortices propagated from their bodies.

2.7.2 Ostraciidae Hydrodynamics

Much of the hydrodynamic studies of this family of fish are in the context of bio-inspired robotics. A study performed by Bartol *et al*. [28] from UCLA explored the role of the rigid carapace on self correcting instabilities. They used smooth trunkfish (Ostraciidae Lactophyrs Triqueter) at different angles of attack to oncoming flow. The flow patterns, forces, and moments were recorded using digital particle image velocimetry (DPIV).

This group found that at positive pitching angles of attack, vorticity began to develop near the anterior edges of the ventro-lateral keels near the eye ridge. As the vortices traveled down the ventro-lateral keel of the fish, it intensified into two well-developed, counter-rotating vortices. The vortices left the body at the caudal preduncle region.

The group noted that regions of concentrated vorticity formed above the ventro-lateral keel. At negative pitching angles of attack, the same vorticity formation and shedding is observed, but the concentrated vorticity above the ventro-lateral keel now appeared below the ventro-lateral keel. A further observation at negative angles was that switching of vortical flow rotation [28].

It was concluded that the anterior origins of the ventro-lateral keels force flow separation and the generation of vorticity during pitching and yawing. Since the ventro-lateral keel extends along the majority of the body, it provides a large area for vorticity buildup when coupled with the regions of lateral concavity above and ventral concavity below the ventro-lateral keel. These regions act as channels for vorticity development. As a result of the vortical development along the carapace, the smooth trunkfish can self-correct for water disturbances [28].

In the same family as the smooth trunkfish, is the boxfish (Ostraciidae). Kodati *et al.* [29] of University of Delaware, used the boxfish as a basis for the design of an autonomous underwater vehicle (AUV). The group performed a study on different morphological parameters responsible for the stability of the boxfish. To accomplish this, the group modeled relative approximations of boxfish and analyzed the flow around the model using computational fluid dynamics (CFD).

Bartol *et al.* concluded that there are two shape factors responsible in altering vortex generation [28]:

1. Change in the cross-section profile. Change along the body affects pitch stability and change across the body affects yaw stability
2. Sharpness of the keels related to the concavity and convexity of the joining faces.

The group found that if the cross sectional area gets significantly higher suddenly, then the peak vorticity will be higher for all angles of attack. Concerning the second point, as the sides of the model become more concave, the vorticity becomes more

concentrated on the keel than the body region.

2.8 Verdant Power MCT

One commercially available marine current turbine is the Verdant Power Gen5 KHPS turbine. A 3 dimensional model can be seen in Fig. 2.5. Verdant deployed a six-turbine array of their Gen4 turbines in New York Harbor. During tests, they were able to generate 12MWH of grid connected electricity. After these tests, the Gen5 turbine was designed to be a more commercially viable solution.

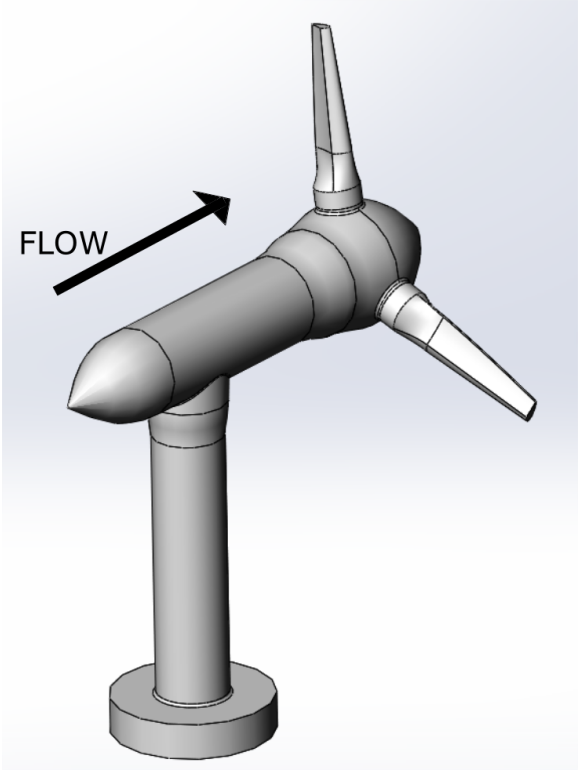

Figure 2.5: 3D Computer Aided Design model of Verdant Power Gen5 Turbine used as a base model for this thesis.

An important aspect of this turbine is that it is a downflow turbine. This means that the turbine is designed so that the water flow flows across the nacelle body before it hits the turbine blade. For this reason, the nacelle geometry can affect the fluid flow to the turbine blade and thus affect the performance of the turbine. It is for this reason

that the Verdant Gen5 was chosen as a base case for this thesis.

3 Design and Analysis of Bio-inspired Nacelle for Current Energy Turbine

3.1 Methodology

The flow of work for this thesis is summarized in the flowchart shown in Fig. 3.1.

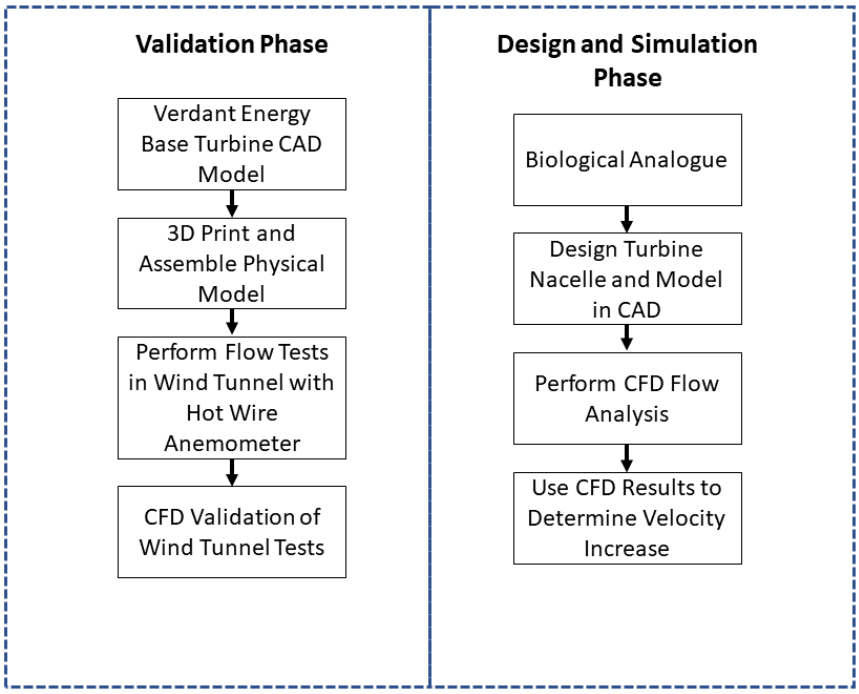

Figure 3.1: Flow chart showing the procedure for evaluating a new turbine design.

The validation phase involved wind tunnel experiments on a 3D printed model and the results from these experiments were used to validate two different types of models used in computational fluid dynamics (CFD). The design and simulation phase involved testing various redesigns of the base model using CFD. No physical testing was performed during this phase.

3.1.1 Validation Phase

In order to validate the CFD model that was used in simulations, a physical model of the base turbine case was 3D printed using Acrylonitrile Butadiene Styrene (ABS). The model as well as a stand were assembled and placed in a wind tunnel for testing.

Figure 3.2 shows the final assembled model and stand inside the wind tunnel. The direction of fluid motion is from the aft end of the model (left in the figure), down the body, and to the turbine blades (right in the figure).

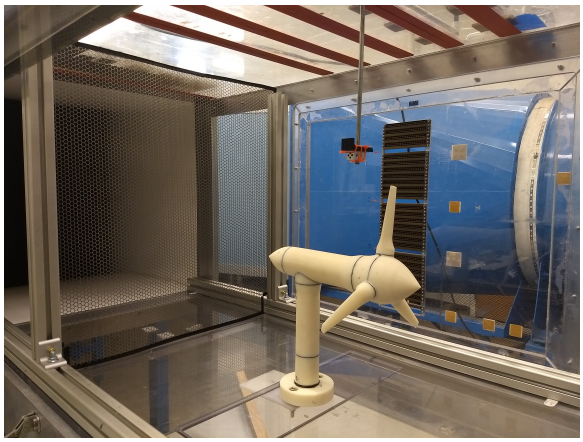

Figure 3.2: Physical model of base case turbine in wind tunnel.

A mesh grating was set up at the fluid inlet to induce a turbulent flow in the wind tunnel. A hot wire anemometer was used to measure the fluid velocity and turbulence intensity at ten randomly chosen points. The locations of these points are all measured with respect to the tip of the aft cone (left in the figure) with the positive y-direction down the body towards the turbine blades. Table 3.1 gives the Cartesian coordinates of the measured point in the order in which they were measured.

To further show where these points are in relation to the actual turbine, Fig. 3.3 shows the measured points in the CFD interface. Each point was measured ten times at three different wind velocities. Table 3.2 gives a summary of the wind tunnel inlet conditions (velocity and turbulence intensities) measured while testing. A grating was used in the wind tunnel inlet to establish a known turbulence during the test.

Two computational fluid dynamic (CFD) models were used in the validation simulations: shear-stress transport (SST) and k-ϵ model. These two models are simulated at the same inlet conditions listed in Table 3.2.

Table 3.1: Mapping of measured points to cartesian coordinates.

Point Number	x-coord. [m]	y-coord. [m]	z-coord. [m]
1	0.0635	-0.165	0.0445
2	-0.0699	-0.165	0.0572
3	0.0255	0.140	0.0560
4	-0.0630	0.164	-0.0170
5	0.1510	0.164	-0.0730
6	0.0150	0.240	0.1370
7	0.0140	0.240	0.0355
8	0.0810	0.240	-0.0140
9	0.0140	0.240	-0.0410
10	0.0220	0.147	0.0440

Table 3.2: Tested wind tunnel velocities and turbulence intensities

Frequency [Hz]	Velocity [$\frac{m}{s}$]	Turbulence Intensity [%]
40	7.959	3.545
52	10.109	3.537
60	11.345	3.587

3.1.2 CFD Settings

The mesh size function was set to proximity and curvature with the mesh relevance center set to fine. The minimum size of the mesh is 0.206920 mm, located at the transition of the turbine body to the fluid domain. Table 3.3 shows some mesh metrics for the base turbine mesh. These metrics were nearly identical for all other cases.

Table 3.3: Mesh metrics for base case turbine.

Mesh Metric	Average	Max	Min
Element Quality	0.7971	0.9994	3.584e-2
Aspect Ratio	1.9690	48.848	1.162
Skewness	0.2921	0.9879	1.464e-4
Orthogonal Quality	0.7063	0.9911	1.210e-2

In Fluent, the method was set to either k-omega with the model being SST, or k-epsilon using a realizable wall function. The fluid was set to the parameters listed for seawater in Table 3.4. The solid material was set to a density of 1070 $\frac{kg}{m^3}$. The solution

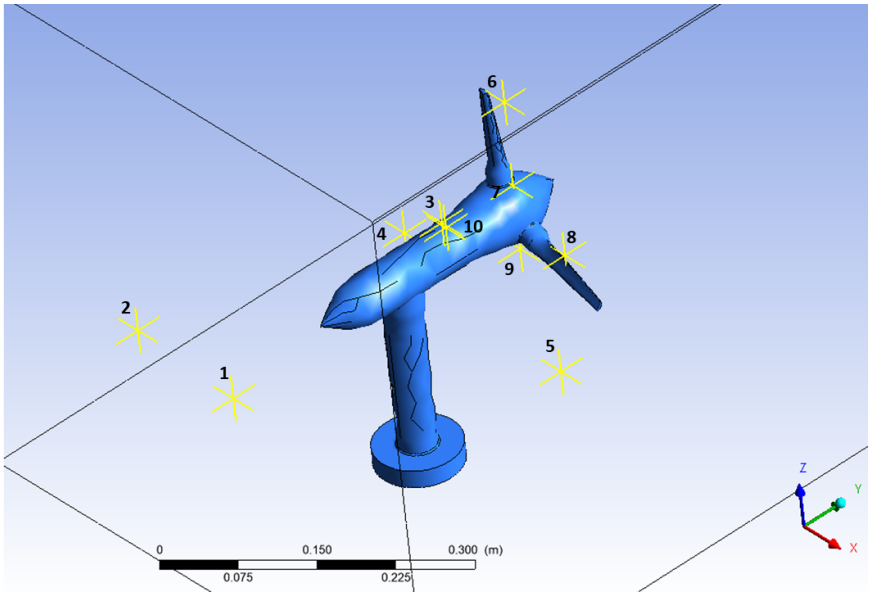

Figure 3.3: Pictoral mapping of measured points to cartesian coordinates.

method was set to coupled with no other changes. The results of the simulations at each of the 10 validation points are shown in Figs. 3.4-3.6. These figures show the comparison between the data taken using a hot wire anemometer (HWA) during wind tunnel testing and the two CFD methods used.

The figures show that there is a good agreement with both CFD models and the measured velocities. The only discrepancy is at point 8 which is located at the edge of the turbine blade. The rest of the points are all within the measured uncertainty of the hot wire anemometer which is derived in Appendix A. The results for the turbulent intensity validation show more discrepancy than the velocity results. From prior experiments, the turbulence intensity of the wind tunnel is known to decay with increasing distance from the inlet. The CFD results show that the models overestimate the turbulence intensity for the points farthest from the fluid inlet. Taking into account this decay can explain this overestimation. This thesis is centered around increasing fluid velocity, therefore, the results are acceptable to continue with future experiments.

The wind tunnel tests were performed using air, but the operating fluid for the rest

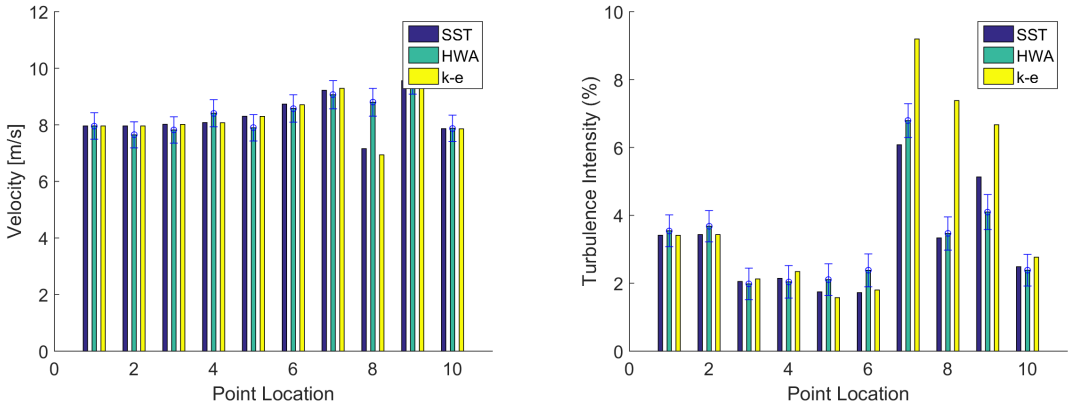

(a) (b)

Figure 3.4: (a) Velocity comparison for inlet velocity of 7.959$\frac{m}{s}$. (b) Turbulence intensity comparison for inlet velocity of 7.959$\frac{m}{s}$. The error bars represent the error associated with the HWA and are derived in Appendix A.

of the simulations is water. For this reason, the Reynolds number for both cases needs to be compared. Consider a horizontal rectangular duct of water with square cross section of 0.6096 m. The Reynolds number for this is given by the following equation:

$$Re = \frac{\rho v D_H}{\mu}$$

where ρ is the density of the fluid, v is the velocity of the fluid, D_H is the hydraulic diameter defined by $D_H = \frac{4A}{P}$ where A is the cross-sectional area and P is the inside perimeter, and μ is the dynamic viscosity of the fluid. Table 3.4 shows the properties used for both fluids as well as the calculated Reynolds Number. It is shown that the Reynolds number for the lowest velocities tested for both fluids are on the same order of each other. This means that the CFD simulation should be valid for both fluids.

The final step in this phase was to test the two CFD methods against each other. Both methods were run at a freestream of 1.5$\frac{m}{s}$ and their velocity and turbulence intensity are calculated and compared in Fig. 3.7. The figure shows that the $k - \epsilon$ method overestimates the turbulence intensity. This is consistent with the results of [23] and

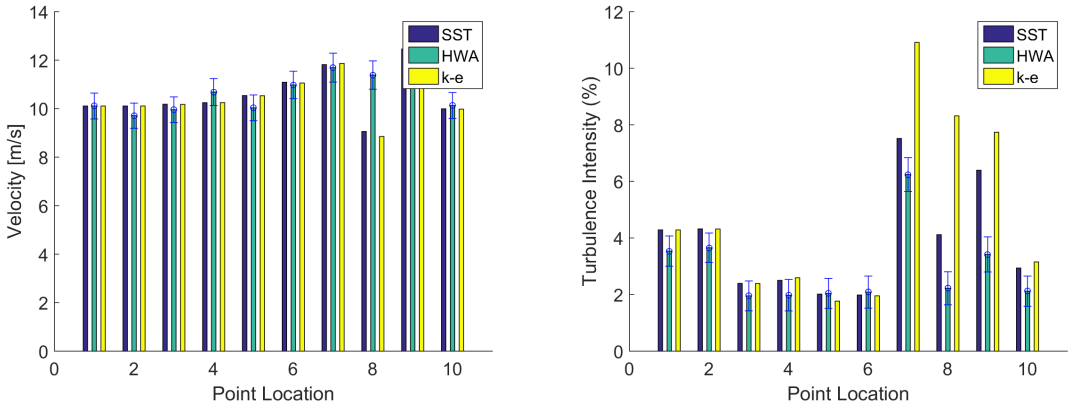

(a) (b)

Figure 3.5: (a) Velocity comparison for inlet velocity of 10.109$\frac{m}{s}$. (b) Turbulence intensity comparison for inlet velocity of 10.109$\frac{m}{s}$. The error bars represent the error associated with the HWA and are derived in Appendix A.

Table 3.4: Tested wind tunnel velocities and turbulence intensities

Property	Seawater	Air
ρ	1025.7	1.225
v [$\frac{m}{s}$]	1	7.959
μ [$\frac{kg}{ms}$]	1.225e-3	1.7894e-5
Reynolds Number	5.1042e5	3.3214e5

is the reason the SST method was developed. For this reason, the SST method was chosen for all simulations.

The results of the validation show that both the SST and $k-\epsilon$ model are candidates for this type of study, but that turbulent intensity is overestimated when using the $k-\epsilon$. It is recommended to use the SST method when performing a study like this one.

3.1.2.1 Design and Simulation

The base model was tested against three newly designed models: a design based on a box fish (Ostraedaii), a design based on a sail fish (Istiophorus), and a design based on the OpenHydro diffuser augmented marine current turbine [30]. Figs. 3.8 shows the 3D

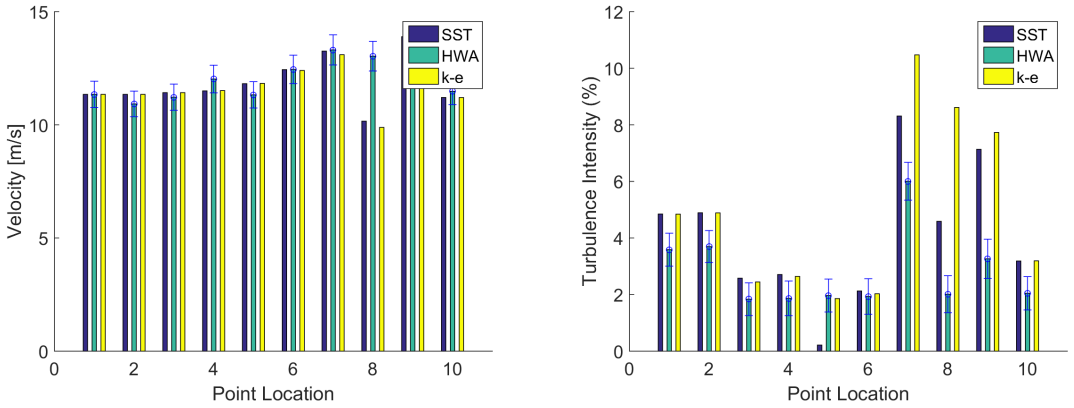

(a) (b)

Figure 3.6: (a) Velocity comparison for inlet velocity of 11.345$\frac{m}{s}$. (b) Turbulence intensity comparison for inlet velocity of 11.345$\frac{m}{s}$. The error bars represent the error associated with the HWA and are derived in Appendix A.

computer aided design (CAD) models used as the test models for the simulations.

Each model is tested at 3 different velocities: 1$\frac{m}{s}$, 1.5$\frac{m}{s}$, 2$\frac{m}{s}$.

3.2 Results

The results of the four models can be seen in Figs. 3.9-3.11 which show the velocity at the inlet of the blade. The data slices were taken to be 10 mm from the top of the blade and 40 mm in front of the blade. The reason that 40 mm was chosen is due to the no-slip condition on the blade surface and the need for the bulk fluid velocity incident on the blade in accordance with the BEM method outlined in section 2.6.4. The height of the sample is set to be the remaining height of the blade. Table 3.5 shows the average percent difference between the 3 designed turbines and the base turbine for the three inlet velocities tested.

Figures 3.9-3.11 show that there is only a marginal velocity increase of the bio-inspired designs with respect to the base turbine. A possible explanation is that the turbines do not possess fins to position the incoming shed vortexes. As outlined in the section on fish hydrodynamics (2.7.1), fish use their fins to position vortex shed from their

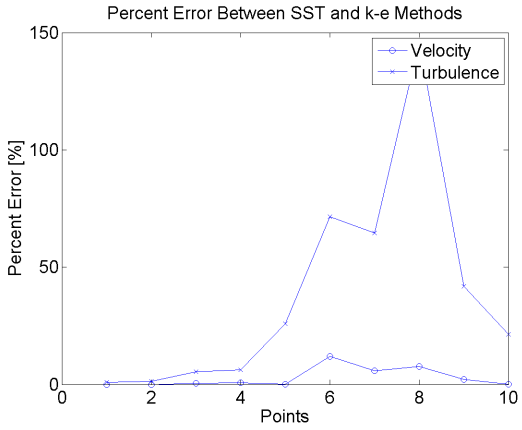

Figure 3.7: Comparison of results for the SST method vs. the $k - \epsilon$ method. The output is in percent difference of the $k - \epsilon$ from the SST method.

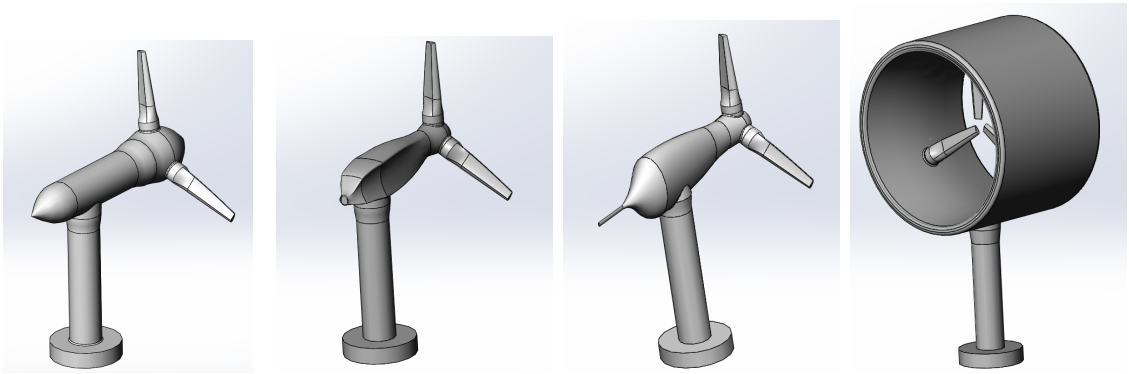

(a) (b) (c) (d)

Figure 3.8: 3D render of the four designed models: (a) Base Case; (b) box fish; (c) sail fish; (d) Diffuser.

bodies. The interaction between the re-positioned vortices is what assists in propulsion. Incorrectly positioned vortices can further explain the unusual shape of the velocity data. A vortex moving in the opposing direction of velocity can decrease local velocities for certain chords of the blade.

An approximate assessment of the additional power provided by each design can be obtained by utilizing equation 2.8 and integrating the local velocities for the whole span

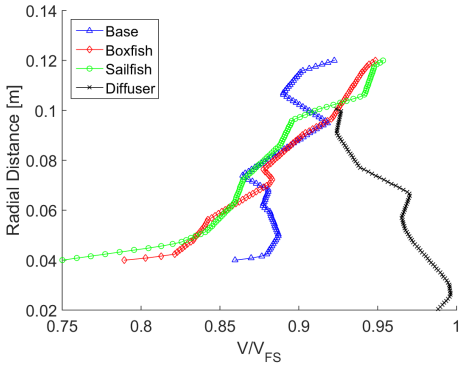

Figure 3.9: Blade velocity comparison between four turbine designs at $1\frac{m}{s}$ inlet velocity normalized by free stream velocity.

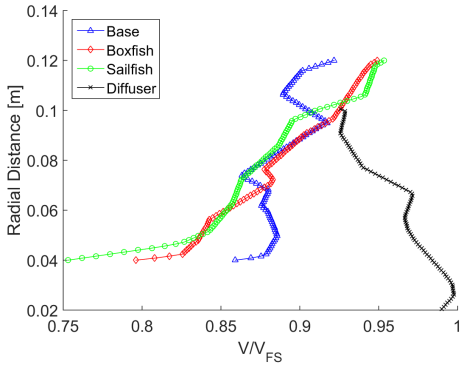

Figure 3.10: Blade velocity comparison between four turbine designs at $1.5\frac{m}{s}$ inlet velocity normalized by free stream velocity.

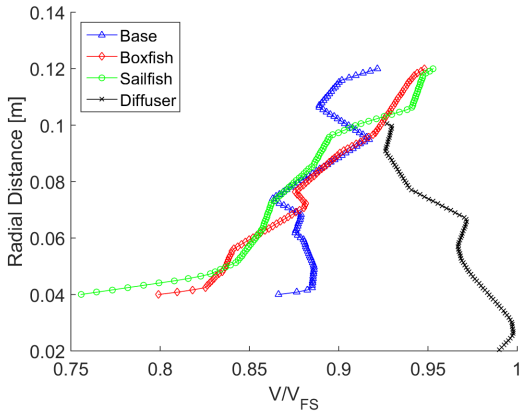

Figure 3.11: Blade velocity comparison between four turbine designs at $2\frac{m}{s}$ inlet velocity normalized by free stream velocity.

of the blade using the following equation:

$$\int_0^L V(r)^2 r dr$$

This equation gives a pseudo estimate of power for the blade. Taking the ratio of the base turbine with a design turbine gives the relative power of the design with respect to the base. Table 3.6 shows the ratios at the three tested inlet speeds. Fig. 3.12 shows the graphical representation of the relative power difference with respect to the base turbine case.

Table 3.5: Percent difference of velocity at the blade between base case turbine and designed models.

Design	$1\frac{m}{s}$	$1.5\frac{m}{s}$	$2\frac{m}{s}$
Box Fish	3.39%	2.67%	3.54%
Sail Fish	3.80%	3.07%	3.9%
Diffuser	15.33%	7.98%	15.75%

Table 3.6: Power increase ratios for three tested inlet fluid velocities relative to the base turbine case.

Design	$1\frac{m}{s}$	$1.5\frac{m}{s}$	$2\frac{m}{s}$
Box Fish	2.82%	3.12%	2.81%
Sail Fish	2.03%	2.10%	2.02%
Diffuser	-32.5%	-32.14%	-32.06%

The table shows that the box fish design gives the greatest gain in terms of relative power. The sail fish design performs better than the base case but marginally less than the box fish case. For all three velocities, the diffuser case performs worst than the base case. This is attributed to the geometry used for the diffuser case. From the comparison plots, figures 3.9-3.11, the fluid velocity decreases for increasing radial distance from the center. A design that is a horizontal axis marine current turbine with a diffuser over it would be a better comparison.

It should be noted that these results are not an exact comparison. There is a difference in hub diameter between the base case and the bio-inspired turbines, where the base case hub is larger than either the box fish or sail fish designs. The data was taken at the same radial distances from the hub in all three cases, but this means that the data for the box fish and sail fish designs is farther up the blade than for the base design. For a more accurate comparison, the hub diameters will need to be the same and the data taken from the same radial distances.

Neglecting radial distance discrepancies, the results show that body geometry can be used to increase fluid velocities, even for lower inlet velocities. This conclusion stems

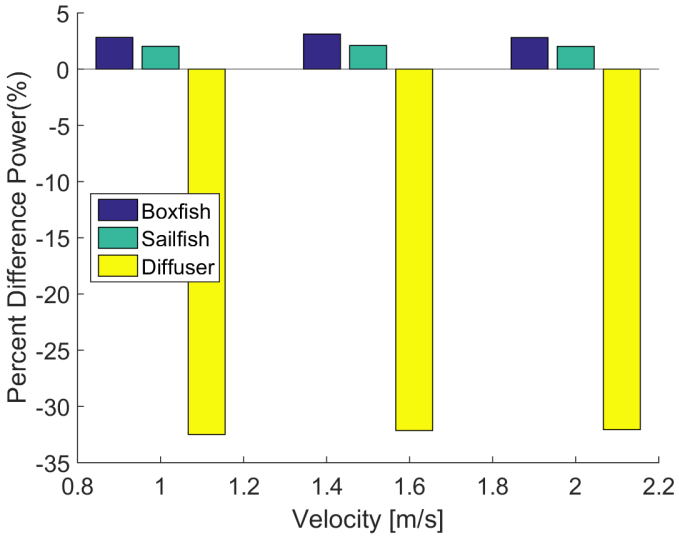

Figure 3.12: Relative power difference with respect to the base model turbine.

from a direct comparison between the box fish and sail fish designs, which have the same hub diameter. Furthermore, the comparison of the diffuser design with the other models shows that a drastic change in body geometry can significantly affect fluid flow. These results are promising because many sites have low average fluid velocities. An example of this is shown in figure 1.3, where the average speed of a current in the waters outside San Francisco, California are below $1\frac{m}{s}$. This makes the box fish design a promising candidate for further research.

To get an idea of the relative cost associated with each design, the mass is estimated using each design's CAD model. The reason that mass is chosen is because material is sold by the metric ton which is 1000 kg. The ratio is then calculated with respect to the base turbine to achieve an estimate of the relative costs, which are shown in Table 3.7. Fig. 3.13 shows a graphical representation of the relative material cost difference between the different designs with respect to the base turbine case.

The table shows that both bio-designed models would be cheaper to build than the base model. The diffuser would cost almost 3.67 times more to build than the base

Table 3.7: Estimated cost of building compared to base turbine design.

Design	Cost of Building
Box Fish	72.48%
Sail Fish	84.48%
Diffuser	367.0%

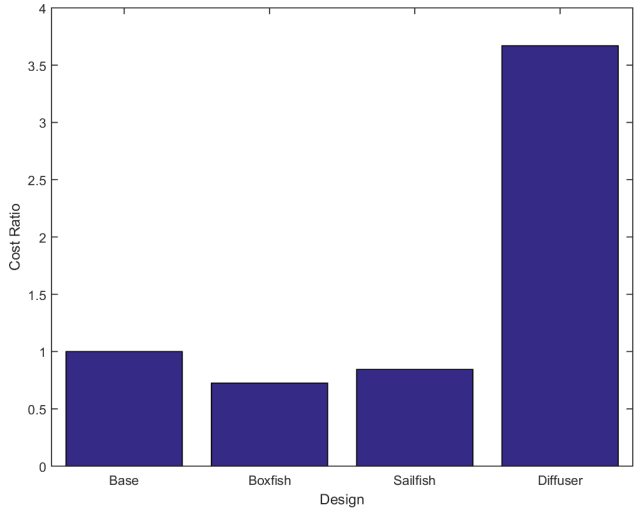

Figure 3.13: Relative material cost ratio with respect to the base model turbine.

model. This is consistent with current industry trends because the diffuser itself needs to be sufficiently elongated in order to increase the velocity. Furthermore, the diffuser is expensive to manufacture due to the low tolerances needed between the blade tip and the shroud. This is mitigated in the design tested, with most of the cost arising from the added material and size of the diffuser. It should be noted that once the hub diameters for the two bio-inspired designs is increased to that of the base case, the percentages in Table 3.7 for the biological designs will increase.

3.3 Conclusion

The shear-stress transport model in computational fluid dynamics was validated with experimental wind tunnel data using a 3D printed model. This method was used to test three different designs for a novel marine current turbine. Of the three models,

two were based on biological analogues and one was based on a utilizing a diffuser. The validated CFD model can further be used to test designs in future research.

The box fish and sail fish design showed performance improvements over the base turbine case. The box fish design showed an average relative power increase of 2.92% in an inlet velocity range of $1\frac{m}{s}$ to $2\frac{m}{s}$. Similarly, the sail fish design showed an average power increase of 2.05%. The diffuser design under performed, compared to all three of the other designs, with an average power decrease of 32.23%, but is due to the design of the blades on the diffuser shroud vice on a hub in the middle.

These results show that a change in nacelle geometry can effect relative performance. The box fish design is seen outperforming the other designs at lower flow velocities. This is significant because ocean currents are often lower than the velocities tested. This shows promise for further research into how nacelle geometry can be exploited at lower flow velocities, as well as how it compares to current solutions. Further exploration into optimizing nacelle geometry will yield greater fluid velocities at the inlet of the turbine blades.

In terms of the material cost to build such a turbine, the bio-designs were marginally less at 72.2% and 84.4% for the box fish and sail fish designs, respectfully. The diffuser based design would cost around 367% times more to build than the base design, demonstrating that a bio-inspired turbine can cost less to build and can perform better than a commercially available design.

LIST OF REFERENCES

[1] International Energy Agency. "IEA, International Energy Agency World Energy Outlook 2017". http://www.iea.org/weo2017/. 2017-11-14.

[2] U.S. Bureau of Ocean Energy Management. "Technology White Paper on Ocean Current Energy Potential on the U.S. Outer Continental Shelf." 2006. https://www.boem.gov/Ocean-Current-White-Paper-2006/. 2017-08-12.

[3] U.S. National Data Buoy Center. "Data For Buoy Station 46026." 2012. http://www.ndbc.noaa.gov/station_page.php?station=46026. 2017-08-12.

[4] S.A.H. Jafari and B. Kosasih. "Flow Analysis of Shrouded Small Wind Turbine with a Simple Frustum Diffuser with Computational Fluid Dynamics Simulations". *Journal of Wind Engineering and Industrial Aerodynamics*, vol. 125:pp. 102–110, 2014.

[5] M.I. Yuce and A. Muratoglu. "Hydrokinetic Energy Conversion Systems: A Technology Status Review". *Renewable and Sustainable Energy Reviews*, 43:72–82, 2015.

[6] M.S. Guney and K. Kaygusuz. "Hydrokinetic Energy Conversion Systems: A Technology Status Review". *Renewable and Sustainable Energy Reviews*, 14.9:2996–3004, 2010.

[7] K. Ng et al. "2002-2012: 10 Years of Research Progress in Horizontal-Axis Marine Current Turbines". *Energies*, 6.3:1497–1526, 2013.

[8] J. Hardisty. *The Analysis of Tidal Stream Power*. Chichester, UK, 2009.

[9] S. Giorgi and J.V. Ringwood. "Can Tidal Current Energy Provide Base Load?". *Energies*, 6:2840–2858, 2013.

[10] S.E. Ben Elghali et al. "Modelling and Control of a Marine Current Turbine-Driven Doubly Fed Induction Generator". *IET Renewable Power Generation*, 4.1:1–11, 2010.

[11] Y. Gu et al. "Corrosion and Protection of Submarine Metal Components in Seawater". *Proceedings of 2009 8th International Conference on Reliability, Maintainability and Safety*, 1:1226–1229, 2009.

[12] Marine Current Turbines. "SeaGen Environmental Monitoring Programme." 2011. http://www.marineturbines.com/sites/default/files/SeaGen-Environmental-Monitoring-Programme-Final-Report.pdf. 2017-08-12.

[13] I.G. Bryden et al. "Tidal Current Resource Assessment". *Proc. Inst. Mech. Eng. A J. Power Energy*, 221:125–135, 2007.

[14] C. Garrett and P. Cummins. "Generating Power from Tidal Currents". *Journal of Waterway, Port, Costal and Ocean Engineering*, 130:114–118, 2004.

[15] L. Myers and A.S. Bahaj. "Power Output Performance Characteristics of a Horizontal Axis Marine Current Turbine". *Renewable Energy*, 31:197–208, 2006.

[16] W.M.J. Batten et al. "Hydrodynamics of Marine Current Turbines". *Renewable Energy*, 31:249–256, 2006.

[17] A.S. Bahaj et al. "Power and Thrust Measurements of Marine Current Turbines Under Various Hydrodynamic Flow Conditions in a Cavitation Tunnel and a Towing Tank". *Renewable Energy*, 32:407–426, 2007.

[18] N. Mehmood et al. "Diffuser Augmented Horizontal Axis Tidal Current Turbines". *Research Journal of Applied Sciences, Engineering and Technology*, 4.18:3522–3532, 2012.

[19] M. Shives and C. Crawford. "Developing and Empirical Model for Ducted Tidal Turbine Performance Using Numerical Simulation Results". *Proc. Inst. Mech. Eng. A J. Power Energy*, 226:112–125, 20011.

[20] A. Bejan. *Convection Heat Transfer*. Wiley, 2013.

[21] A. Muratoglu and M.I. Yuce. "Design of a River Hydrokinetic Turbine using Optimization and CFD Simulations". *Journal of Energy Engineering*, 143, 2017.

[22] M.J. Lawson et al. "Development and Verification of a Computational Fluid Dynamics Model of a Horizontal-axis Tidal Current Turbine". *Proceedings of the International Conference on Offshore Mechanics and Arctic Engineering*, 5:711–720, 2011.

[23] F.R. Menter. "Two-Equation Eddy-Viscosity Turbulence Models for Engineering Applications". *AIAA Journal*, 32:1598–1605, 1994.

[24] R. Mikkelsen. *"Actuator Disc Methods Applied to Wind Turbines"*. PhD thesis, Technical University of Denmark, Nils Koppels All, Building 403, Technical University of Denmark , DK-2800 Lyngby, Denmark, 7 2003.

[25] T. Javaherchi et al. "Hierarchical Methodology for the Numerical Simulation of the Flow Field around and in the Wake of Horizontal Axis Wind Turbines: Rotating Reference Frame, Blade Element Method and Actuator Disk Model". *Wind Engineering*, 38.2:181–201, 2014.

[26] M.J. Lighthill. "Aquatic Animal Propulsion of High Hydromechanical Efficiency". *Journal of Fluid Mechanics*, pages 265–301, 1970.

[27] M.S. Triantafyllou et al. "Hydrodynamics of Fishlike Swimming". *Annual Review of Fluid Mechanics*, 32.

[28] I.K. Bartol et al. "Hydrodynamic Stability of Swimming in Ostraciid Fishes: Role of the Carapace in the Smooth Trunkfish Lactophrys Triqueter (Teleostei: Ostraciidae)". *Journal of Experimental Biology*, 206.

[29] P. Kodati et al. "Microautonomous Robotic Ostraciiform (MARCO): Hydrodynamics, Design, and Fabrication". *IEEE Transactions on Robotics*, 24.

[30] Open Hydro Inc. "EDF PaimpolBréhat." 2017. `http://www.openhydro.com/Media-Centre/Pictures/Gallery-One`. 2017-08-12.

[31] R.S. Figliola and D.E. Beasley. *Theory and Design for Mechanical Measurements*. Wiley, 2006.

[32] F.E. Jorgenson. "How to Measure Turbulence with Hot-wire Anemometers - A Practical Guide." 2002. `http://web.iitd.ac.in/~pmvs/courses/mel705/hotwire2.pdf`. 2017-08-12.

A Appendix

A.1 Error Propagation

The equation for uncertainty for a measurement made with the hot wire anemometer is governed by the following equation:

$$U_V^2 = \left(\frac{\partial V}{\partial \Delta P} u_{\Delta P}\right)^2 + \left(\frac{\partial V}{\partial \rho}\frac{\partial \rho}{\partial T_{amb}} u_{T_{amb}}\right)^2 + \left(\frac{\partial V}{\partial \rho}\frac{\partial \rho}{\partial P_{amb}} u_{P_{amb}}\right)^2 + (u_{fit})^2 + \left(\frac{\partial V}{\partial E} u_E\right)^2 + \left(\frac{\partial V}{\partial \theta} u_\theta\right)^2$$

where U_V is the uncertainty in velocity for a voltage measured by the anemometer. V represented the velocity measured by the anemometer, ΔP is the differential pressure measured by the pitot tube, ρ is the density of the fluid, T_{amb} is the ambient temperature during the measurement, P_{amb} is the ambient pressure during the measurement, E is the voltage measured by the data acquisition board, and θ is the angle of the anemometer.

A.1.1 Differential Pressure Error

The Dantec miniCTA hot wire anemometer used for testing was calibrated using a Pitot tube and a Dwyer Series 475 Mark 3 differential pressure meter. The differential pressure meter has an uncertainty of $\pm 0.5\%$ full scale. In this case, the full scale is 2.491kPA differential. This means that a differential pressure measurement taken with this equipment has an uncertainty of ± 0.012455 kPA as is read from the meter.

The error from the pitot tube occurs in the conversion of the differential pressure into velocity. Since the pitot tube was used in the calibration of the anemometer, it must be taken into account. The contribution to uncertainty for this measurement is represented in the above equation by the following terms:

$$\left(\frac{\partial V}{\partial \Delta P} u_{\Delta P}\right)^2$$

Recalling that the following equation is used to change the differential pressure of a pitot tube into a velocity:

$$V = \sqrt{\frac{2\Delta P}{\rho}}$$

Taking the derivative of this with respect to differential pressure gives:

$$\frac{\partial V}{\partial \Delta P} = \frac{1}{2}\sqrt{\frac{2}{\rho}}\left(\Delta P\right)^{-\frac{1}{2}} = \sqrt{\frac{1}{2\rho\Delta P}}$$

It should be noted that this equation depends on the specific velocity of the fluid and will be different for each velocity. Due to the accuracy of the digital manometer used in reading the differential pressure, the uncertainty of a differential pressure reading is: $u_{\Delta P} = \pm 12.455$ Pa.

A.1.2 Density Error

Changes in ambient pressure and ambient temperature both effect the density of air. In the above equation, this is represented in the terms:

$$\left(\frac{\partial V}{\partial \rho}\frac{\partial \rho}{\partial T_{amb}}u_{T_{amb}}\right)^2 + \left(\frac{\partial V}{\partial \rho}\frac{\partial \rho}{\partial P_{amb}}u_{P_{amb}}\right)^2$$

The first term for each is derived from the equation to convert pitot tube differential pressure to velocity. Taking the derivative with respect to density vice differential pressure gives:

$$\frac{\partial V}{\partial \rho} = -\frac{1}{2}\sqrt{2\Delta P}\rho^{\frac{3}{2}} = \sqrt{\frac{\Delta P}{2\rho^3}}$$

the next term is derived by using the following equation for density: $\rho = \frac{P}{RT}$. The partial derivative with respect to temperature gives:

$$\frac{\partial \rho}{\partial T_{amb}} = \frac{-P}{RT^2}$$

Using the same equation, the derivative with respect to pressure gives:

$$\frac{\partial \rho}{\partial P_{amb}} = \frac{1}{RT}$$

The terms $u_{T_{amb}}$ and $u_{P_{amb}}$ depend on instruments for measuring. These are estimated to be 1^oC and $10kPa$ respectively.

A.1.3 Calibration Error

Calibration error is contained in the term u_{fit} and arise from the way the hot wire anemometer is calibrated. As per the Dantec miniCTA hot wire anemometer instruction manual, a pitot tube is used to calibrate the anemometer. The process start with pitot tube measurements taken alongside anemometer voltages for various wind tunnel motor frequencies. Wind tunnel frequencies are plotted verus wind velocity and a trend line is fitted to the data. This results is a linear equation in the form of $u = A * frequency + B$.

The second step is to plot anemometer voltage versus velocity using the equation from the previous curve fit. A trend line is fitted to this data to get an equation of the form: $u = Av^2 + Bv + c$ where u is the velocity, v is the voltage, and A,B,and C are coefficients. The uncertainty in this equation is that of the velocity relating to the voltage of the anemometer.

To determine the uncertainty in the polynomial of a linear regression curve fit, there is deviation $y_i - y_{c_i}$ between the data point and the polynomial . First, define ν = N - (m+1) where N is the number of data points and m is the order of the curve fit. The equation for the standard deviation from the curve fit is [31]:

$$S_{yx} = \sqrt{\frac{\sum_{i=1}^{N} (y_i - y_{C_i})^2}{\nu}}$$

where y_i is a measured data point, y_{C_i} is the same data point from the polynomial

curve fit, and ν is defined above.

If variability in both the dependent and independent variable are to be considered, then the uncertainty is given by the following equation [31]:

$$\pm t_{v,P} S_{yx} \left[\frac{1}{N} + \frac{(x - \bar{x})^2}{\sum_{i=1}^{N} (x_i - \bar{x})^2} \right]^{\frac{1}{2}}$$

where:

$$\bar{x} = \sum_{i=1}^{N} x_i$$

the variable $t_{\nu,P}$ is known as the Student's T-distribution. It is a known distribution in statistics. For the case of the hot wire anemometer uncertainty, the distribution for 95% interval was taken.

A.1.4 Voltage Error

The uncertainty in the voltage is encapsulated in the term:

$$\left(\frac{\partial V}{\partial E} u_E \right)^2$$

The velocity measured by the anemometer with respect to voltage is given by the polynomial curve fit equation $V = a_1 E^2 + a_2 E + a_3$. Taking the derivative of this equation with respect to voltage E gives:

$$\frac{\partial V}{\partial E} = 2a_1 E + a_2$$

The uncertainty of a voltage measurement, u_E, is derived from the resolution of data acquisition (DAQ) used. The equation for this term is given by:

$$u_E = \frac{VoltageRange}{2^N}$$

where voltage range is the total range of voltages measured, which was ± 10 volts giving 20V, and N is the resolution in bits. The National Instruments Universal Serial Bus 6009 (NI USB-6009) was used which has a resolution of 13 bits for a single ended measurement. Using this information in the above equation:

$$u_E = \frac{20V}{2^{13}}$$

A.1.5 Angle Error

Angle error is due to the anemometer being at a angle that isn't exactly parallel with oncoming fluid flow. It contributes to error in the term:

$$\left(\frac{\partial V}{\partial \theta} u_\theta\right)^2$$

The general equation relating angle to voltage for a hot wire anemometer is given by [32]:

$$V = \frac{1}{\sqrt{3}}(1 - \sin\theta)$$

and taking the derivative with respect to θ gives:

$$\frac{\partial V}{\partial \theta} = \frac{1}{\sqrt{3}} \cos\theta$$

The uncertainty of an angle measurement is further given in [32] as $u_\theta = 1^o$.